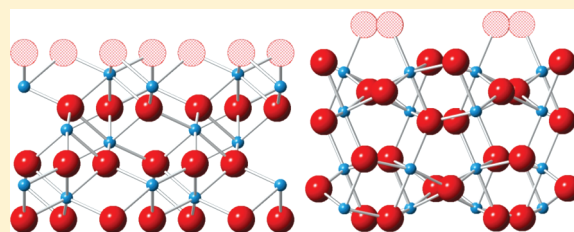


Surface Structure and Reactivity of Rhodium Oxide

Yaniv D. Scherson,^{*,†} Shela J. Aboud,[‡] Jennifer Wilcox,[‡] and Brian J. Cantwell[†][†]Department of Aeronautics and Astronautics, Stanford University, 496 Lomita Mall, Stanford, California 94305, United States[‡]School of Earth Sciences, Stanford University, Stanford, California 94305, United States

ABSTRACT: Density functional theory calculations have been performed in conjunction with ab initio thermodynamics and density of states analysis to investigate the stability and reactivity of the (0001) and (1 $\bar{1}$ 02) Rh₂O₃ surfaces. A total of seven surfaces have been investigated using density functional theory (DFT) and the DFT+*U* extension. DFT and DFT+*U* (*U* = 3.5 eV) predicted nearly identical lattice parameters and similar trends in surface stability and reactivity. Using ab initio thermodynamics, the c-cut and r-cut surfaces were determined to be close in stability and the most thermodynamically stable surfaces were predicted to be among the most reactive. An oxygen-terminated c-cut surface and an oxygen-terminated r-cut surface were found to exhibit high Lewis acidity and to be close in stability at larger oxygen chemical potentials, possibly explaining the high experimentally observed catalytic activity of Rh₂O₃ at low temperatures. As compared to DFT, DFT+*U* predicted a crossover point in surface stability to occur at a larger oxygen chemical potential and predicted surface stability to occur over a wider range of oxygen chemical potential. In this work, Rh₂O₃ exhibited similar trends in surface stability as compared to α -Fe₂O₃ and α -Al₂O₃.



1. INTRODUCTION

Rhodium metal catalysts are used in wide a range of applications, including automotive catalytic converters for NO reduction, N₂O decomposition, and CO oxidation.^{1–7} Theoretical and experimental studies have found that, under realistic environmental conditions, rhodium surfaces can oxidize, forming thin films or thicker bulk oxides.^{8,9} In the case of CO oxidation, it has been shown that the formation of thin film oxides increases the catalytic reactivity of the surface.¹⁰ A variety of phases of rhodium oxide have been found to exist: corundum phase Rh₂O₃ I (space group *R* $\bar{3}$ *c*), corundum phase Rh₂O₃ II (space group *Pbna*), corundum phase Rh₂O₃ III (space group *Pbca*), and rutile phase RhO₂.¹¹ Phase I has been shown to be the most stable phase at low to moderate temperatures (below 1350 °C) and in the pressure range of 0–3.27 GPa.¹¹ Although several studies have investigated the formation of the bulk oxide of the phases of rhodium oxide and the structure of the thin film RhO₂ oxide phase, to our knowledge there have been no detailed density functional theory (DFT) investigations regarding the structure of the stable corundum surface.

Corundum Rh₂O₃ I is isostructural with α -Al₂O₃ and α -Fe₂O₃, differing primarily in the size of the cations and the lattice constant.^{11,12} Previous studies of α -Al₂O₃ and α -Fe₂O₃ have found the surfaces to exist in two forms, one in which the surface is cleaved along the (0001) plane, called the c-cut surface, and the other cleaved along the (1 $\bar{1}$ 02) plane, called the r-cut surface.^{13–18} The configuration of the surface atoms (i.e., whether the structure is more stable with metal cation or oxygen anion termination) is a function of both the temperature and partial pressure of the surrounding environment and has been shown to be a function of catalyst preparation.¹⁹ The surface structure of the oxide

influences its catalytic activity through the distribution of charge and is therefore related to the Lewis acidity of the surface sites.

The goal of this work is to use DFT to understand the most thermodynamically stable surfaces of the corundum phase I of Rh₂O₃ under different temperature and pressure environments. However, application of the DFT approach to highly correlated metal oxides can lead to errors in the calculation of the electron self-interaction; unpaired electrons will tend to delocalize over many atoms and reduce the Coulomb repulsion. The self-interaction error can lead to errors in the calculated band structure, typically resulting in a smaller predicted band gap that can translate into incorrect predictions in the magnetic properties, surface stability, and surface catalytic reactivity. In the case of α -Fe₂O₃, DFT can even predict the incorrect insulator type.^{20,21} Experimental measurements and theoretical predictions have shown Fe₂O₃ to be a charge-transfer-type material in which the band gap is formed through the 3d valence band states of the Fe cations and the 2p conduction band states of the oxygen anions.²² Simulations using DFT, on the other hand, predict Fe₂O₃ to be a d–d Mott–Hubbard insulator.^{21,23} While this difference in the structure of the conduction band states between experiment and DFT will impact properties related to the excited states of the electrons, the role this difference plays in surface stability and catalytic reactivity remains unclear.

One approach to correct for the electron self-interaction error within local density approximation (LDA) and generalized gradient approximation (GGA) is the application of DFT+*U*,

Received: November 17, 2010

Revised: April 10, 2011

Published: May 16, 2011

which was specifically developed for 3d-transition-metal oxides.²⁴ DFT+*U* explicitly includes an effective local two-electron repulsion term, *U*, to correct the self-interacting energy. The approach has been shown to correct the predicted band gap and heats of formation in bulk material by tuning the *U* parameter. However, this approach is limited by relying on an effective parameter whose value is not based on any fundamental physical properties. Furthermore, there is still debate on whether applying an effective *U* parameter derived from the bulk structure to surface atoms is valid for predicting adsorption energies and activation barriers used to describe the chemical kinetics of surface phenomena such as diffusion or reactivity.²⁵

Alternatives to DFT+*U* are the hybrid functionals, which include contributions from the exact Fock exchange and pure density functionals.^{26,27} Hybrid functionals are considered an improvement over DFT+*U*; however, since they also rely on calibrated parameters, specifically the amount of the Fock exchange term, caution must be exercised when interpreting results. Furthermore, hybrid functionals can be much more computationally intensive than DFT+*U*, thus making large oxide simulations time-prohibitive.^{28,29} Previous work shows reasonable agreement between calculations using a hybrid functional and those using DFT+*U* as applied to bulk CeO₂ and Ce₂O₃,³⁰ suggesting DFT+*U* generally offers a compromise between accuracy and computational cost.

In this work, the stability and reactivity of four r-cut and three c-cut surface terminations of phase I Rh₂O₃ are examined under varying environmental conditions. The temperature and oxygen partial pressure are principal environmental parameters that dictate surface stability, structure, and reactivity. Using ab initio thermodynamics, the relative stability of the surfaces investigated have been calculated using DFT and DFT+*U* and expressed as a function of the oxygen chemical potential. Comparisons in surface stability and reactivity are made between DFT and DFT+*U*, and the reactivities of the most thermodynamically stable surfaces are further investigated through calculations of the Lewis acidity. Density of states, Bader charge, and bond valence calculations also yield further insight into reactivity.

2. METHODOLOGY

2.1. Density Functional Theory. Density functional theory calculations were performed using the Vienna ab initio Simulation Package (VASP)³¹ with the projector augmented wave (PAW) method³² to describe the ion–electron interactions. Electron exchange–correlation functionals were represented with the GGA, and the model of Perdew, Burke, and Ernzerhof (PBE)³³ was used for the nonlocal corrections. A plane-wave expansion cutoff of 450 eV was applied, and the surface Brillouin zone integration was calculated using a γ -centered $5 \times 5 \times 5$ ($5 \times 5 \times 1$ for the surface) Monkhorst–Pack mesh.³⁴ Methfessel and Paxton³⁵ Gaussian smearing of order 1 with a width of 0.2 eV was used to accelerate the convergence of the total energy calculations. Geometric optimization was performed using the conjugate-gradient algorithm until the absolute value of the forces on unconstrained atoms was less than 0.03 eV/Å. In this work, GGA greatly underpredicted the band gap of Rh₂O₃ (predicted $E_g = 0.2$ eV vs experimental $E_g = 1.20$ eV); therefore, the GGA+*U* extension was applied. The DFT+*U* approach adds a correction factor to the total energy equation that is calibrated to more accurately predict the electronic and material properties of Rh₂O₃.^{36,37} In this work, *U* was calibrated to accurately predict

the band gap of Rh₂O₃. Results from the DFT approach with and without *U* are presented.

2.2. Ab Initio Thermodynamics. Ab initio thermodynamics can be used to predict the relative stability between surface terminations under different environmental conditions. In this work, the stability of the seven Rh₂O₃ surface terminations is studied as a function of the oxygen chemical potential. The surface free energy for Rh₂O₃ surfaces as a function of the oxygen chemical potential is defined in the following equation:^{14,38–40}

$$\gamma = \frac{1}{2A} \left[G_{\text{Rh}_2\text{O}_3}^{\text{surface}} - \frac{N_{\text{Rh}}}{2} G_{\text{Rh}_2\text{O}_3}^{\text{bulk}} - \left(N_{\text{O}} - \frac{3}{2} N_{\text{Rh}} \right) \mu_{\text{O}} \right] \quad (1)$$

where *A* is the area of the slab, $G_{\text{Rh}_2\text{O}_3}^{\text{surface}}$ is the free energy of the slab representing the surface, $G_{\text{Rh}_2\text{O}_3}^{\text{bulk}}$ is the free energy of the metal oxide bulk per Rh₂O₃ formula unit, μ_{O} is half of the chemical potential of the gas-phase O₂ molecule, and N_{Rh} and N_{O} refer to the number of metal and oxygen atoms in the slab, respectively. It is assumed that the bulk phonon modes do not change with the creation of the slab nor by the adsorption of oxygen and therefore the bulk phonons in the slab cancel with the vibrational portion of the bulk free energy. Previous work has shown that the oxygen vibrational contributions to changes in energy are within the error of DFT and are therefore omitted.³⁹ In the surface free energy expression above, only μ_{O} varies with temperature and pressure and is expressed in eq 2. The oxygen chemical potential at the reference pressure is obtained from the NIST-JANAF tables.⁴¹

$$\mu_{\text{O}}(T, p) = \mu_{\text{O}}(T, p^{\circ}) + \frac{1}{2} kT \ln \left(\frac{p_{\text{O}_2}}{p^{\circ}} \right) \quad (2)$$

Although the surface free energy expression in eq 1 is continuous over all values of μ_{O} , there is a physical limit to realistic oxygen chemical potentials of interest. In an oxygen-rich environment gas-phase oxygen condenses on the surface, while in an oxygen-poor environment the oxide surface decomposes into bulk rhodium and gas-phase oxygen. The minimum and maximum values of μ_{O} can be expressed as

$$\mu_{\text{O},\text{max}} = \frac{1}{2} E_{\text{O}_2} \quad (3)$$

$$\mu_{\text{O},\text{min}} = \frac{1}{3} E_{\text{Rh}_2\text{O}_3}^{\text{bulk}} - \frac{2}{3} E_{\text{Rh}}^{\text{bulk}} \quad (4)$$

where E_{O_2} is the total energy of the O₂ molecule, $E_{\text{Rh}_2\text{O}_3}^{\text{bulk}}$ is the total energy of bulk Rh₂O₃ per formula unit, and $E_{\text{Rh}}^{\text{bulk}}$ is the total energy of bulk Rh, with all energies calculated at $T = 0$ K.

2.3. Bond Valence. The bond valence model is an empirical measure of Pauling's valence sum rule⁴² relating the electrostatic bond strengths around each ion in a crystal to its valence number. The amount that the total sum of the bond valences differs from the valence number provides a direct measure of the coordination of a given ion in the crystal and provides information about the reactivity. Brown and Altermatt wrote a computer program to search the inorganic crystal structure database and characterize the coordination polyhedral of a large number of cations. They were able to fit the bond valence and bond length data to a simple exponential formula.⁴³ While a range of ionic crystals have been studied, including other corundum oxides, α -Fe₂O₃ and α -Al₂O₃, no data exist for the bond valence parameters of Rh₂O₃. We use

Table 1. Geometric Parameters and Band Gap Energy for Rh₂O₃

	<i>a</i> (Å)	<i>c</i> (Å)	<i>E_g</i> (eV)
DFT, this work	5.20	14.10	0.20
DFT+ <i>U</i> , this work	5.19	14.00	1.14
exptl ^{49,50}	5.13	13.85	1.20
exptl ¹²	5.108	13.81	
DFT ¹⁰	5.13	13.8	
DFT ⁵¹	5.208	14.155	

the DFT results to predict the bond valence parameters for Rh₂O₃ and then use the resulting analysis to understand differences in the structure and stability of Rh₂O₃ with α-Fe₂O₃ and α-Al₂O₃.

The contribution to the total bond valence from each neighboring ion for Rh₂O₃ is given by the expression^{44,45}

$$S_{M-O} = \exp\left(\frac{R_0 - R_{M-O}}{37}\right) \quad (5)$$

where R_{M-O} is the bond distance between rhodium and oxygen and R_0 is 1.817 Å and 1.812 Å as determined from DFT and DFT+*U*, respectively. The total bond valence of a particular ion, *i*, is given by summing the individual contributions from the all-bonded neighboring ions as shown by the expression

$$BV_i = \frac{\text{charge}}{\text{coordination}} = \sum_j S_{i-j} \quad (6)$$

For a particular atom or group of atoms, higher reactivity is correlated to a bond valence that is further away from the corresponding valence number.

The chemical reactivity of a surface can be understood through the acid–base properties, which are governed by the charge distribution of the surface ions and the reactant species. For example, undersaturated surface oxygen atoms of an oxide can possess lone-pair or nonbonded electron density, which leads to significant electron–electron repulsion, while oversaturated surface oxygen atoms will have insufficient density to donate to surrounding bonds, which leads to repulsion between neighboring atoms.⁴⁶ Reactant species tend to adsorb on the under-coordinated metal and/or oxygen atoms of a surface. The coordination of the surface anions and cations can be measured by their bond valence. The bond valence correlates the length and energy of the bonds stemming from nuclear repulsion, electron–nuclear attraction, and electron–electron interactions. In addition to inorganic solids, bond valence has also been used to examine molecular dynamics potential models for water molecules in the liquid phase.⁴⁷ Since DFT tends to optimize a given structure to satisfy the bond valence, the bond valence analysis can be useful in predicting how reactive a surface will be under specific temperature and pressure conditions. Valence sums of bonds reaching ions in known crystals are typically within ±0.1 vu of the actual valence. Larger deviations can be indicators of a poor structure determination or internal stresses.

3. RESULTS AND DISCUSSION

3.1. Bulk. The initial atomic coordinates of the bulk corundum structure of phase I Rh₂O₃ are taken from the experimentally determined coordinates of α-Al₂O₃.⁴⁸ A geometric optimization of the unit hexagonal cell of the Rh₂O₃ structure has been

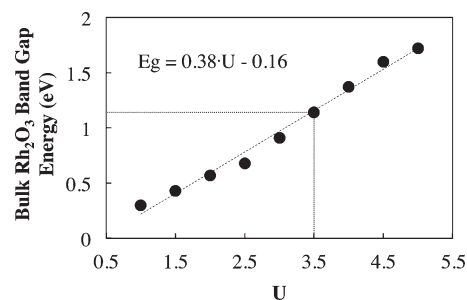


Figure 1. Predicted band gap of Rh₂O₃ vs *U*. *U* = 3.5 eV accurately predicts the true band gap of Rh₂O₃. The dashed line shows the linear best fit with the equation $E_g = 0.38U - 0.16$.

performed by changing the length of each side of the unit cell while holding the other two sides fixed to find the set of lattice constant parameters that minimize the total free energy of the system. The positions of the atomic coordinates are also allowed to relax within the unit cell.

The resulting lattice parameters and the band gap of Rh₂O₃ are shown in Table 1 along with experimental values and results of other DFT calculations of Rh₂O₃. The lattice parameters calculated in this work are slightly greater than 1% compared to experimentally determined values and comparable to other DFT-based studies available in the literature. DFT+*U* predicts slightly smaller lattice parameters as compared to DFT.

DFT greatly underestimates the value of the band gap, 0.20 eV, compared to the experimental value of 1.20 eV. To investigate the influence of an underestimated band gap on the stability and reactivity of the Rh₂O₃ surface, a *U* parameter was chosen to fit the band gap to the experimental value within DFT+*U*. Figure 1 shows a plot of the band gap of Rh₂O₃ for different values of *U*; a value of *U* = 3.5 eV was found to give a reasonable band gap of 1.14 eV. For comparison, previous investigations have applied the DFT+*U* extension to α-Fe₂O₃ with *U* = 3.9 eV²⁵ and *U* = 4.0 eV.²⁴ For each value of *U*, the lattice constants of the unit cell were reoptimized and no significant change was found for the positions of the atomic coordinates of the bulk structure.

The displacement of the metal anions from the geometric center of the octahedral sites of the oxygen ligand depends on neighboring metal–metal repulsion.⁵² In the corundum structure, two metal–oxygen bond lengths exist. For Rh₂O₃, these lengths are 2.03 and 2.07 Å, while for α-Fe₂O₃ these lengths are 1.889 and 2.003 Å.⁵³ The greater symmetry in the Rh₂O₃ structure, as compared to α-Fe₂O₃, suggests fewer metal–metal interactions. Rhodium is more electronegative than iron and as such donates less charge to neighboring oxygen atoms. Therefore, DFT should predict less charge difference on rhodium than iron in the oxide.

The density of states for the bulk rhodium oxide structure is shown in Figure 2 with and without the DFT+*U* extension. The Rh *d* and O *p* orbitals primarily contribute to the density of states over all energies. As compared to DFT, the DFT+*U* extension extends the band gap by shifting the conduction band states to higher energies above the Fermi energy, shown at *E* = 0 eV. However, the DFT+*U* extension also changes the DOS in the valence band.

3.2. Surface Structure Optimization. Previous work has confirmed the stability of the *c*-cut and *r*-cut surfaces of α-Fe₂O₃. However, to our knowledge no work has investigated the stability of these surfaces for Rh₂O₃ as determined by DFT. In this work, a total of seven surfaces were studied with three surfaces from the

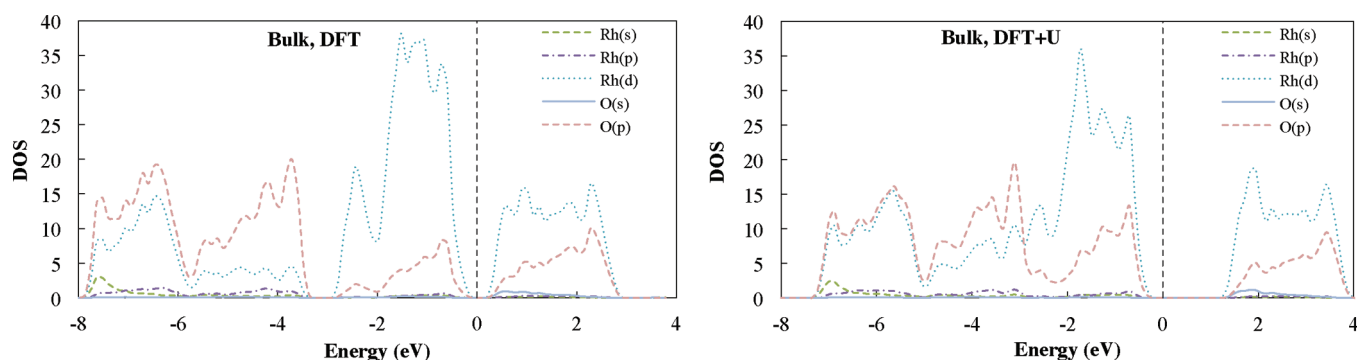


Figure 2. Density of states versus energy with DFT (left) and DFT+ U (right). $E_{\text{fermi}} = 0$ eV in both panels.

c -cut plane (0001) and four surfaces from the r -cut plane ($1\bar{1}02$). Each surface was obtained by cleaving the optimized unit cell of bulk Rh_2O_3 to form a double-sided slab. For the c -cut surface, the bulk oxide was cleaved along the [001] direction, yielding three possible surfaces. The first c -cut surface consists of two rhodium layers followed by an oxygen layer and is referred to as the Rh–Rh- c -cut surface. The second c -cut surface is obtained by removing the top layer of rhodium atoms from the first surface, yielding the Rh–O- c -cut surface. The final c -cut surface is obtained by removing the top rhodium layer from the second c -cut surface and is referred to as the O- c -cut surface. Four r -cut surfaces were obtained by cleaving the bulk oxide along the $[1\bar{1}2]$ direction. Two sets of r -cut surfaces are possible differing only by the order of atomic layers. These are referred to as the pair of r -cutA surfaces and the pair of r -cutB surfaces. The r -cutA and r -cutB surface pairs each contain one surface terminating with two oxygen layers and another surface terminating with an oxygen layer followed by a rhodium layer. The resulting four surfaces are referred to as O–O- r -cutA, O–Rh- r -cutA, O–O- r -cutB, and O–Rh- r -cutB and are shown in Figure 3. In all cases, the final slabs were double-sided, consisting of 20–24 atomic layers, which was deep enough to ensure that the center region of the slab remained bulklike. Additionally, a 30 Å vacuum layer was used to isolate each slab from its periodic image.

The structure of the simulated surfaces was relaxed to allow the layers of each surface to shift into a minimum energy configuration. This results in the displacement of slab layers along the [001] and $[1\bar{1}2]$ directions for the c -cut and r -cut surfaces, respectively.

Tables 2 and 3 show the vertical displacement between slab layers as well as their relative shift in position as compared to the bulk. The distances between atomic layers are shown in angstroms (Δ columns), and the relative shift in layer position is represented as a percent difference (% columns) from the bulk. Furthermore, the results with and without the DFT+ U extension are compared in the table. As can be seen in Table 3, layers closer to the center of the slab experience only a slight shift in vertical position (<1%) as compared to the position in the bulk structure, with the exception of the surfaces O–O- r -cutA and O–Rh- r -cutA in the DFT and DFT+ U cases, respectively, which both show a greater shift in layer position. For reference, Figure 3 shows the numerical designation for each layer.

As compared to the bulk structure, DFT+ U predicts either a comparable or lower percent difference in the slab layer displacement compared to DFT alone. This can be seen by comparing the percent difference column of $U = 0$ eV to $U = 3.5$ eV for each

surface (exception O–O- r -cutA surface), suggesting that the DFT+ U extension may yield more accurate predictions. DFT and DFT+ U shift the layers of the simulated surfaces in the same direction from the bulk structure, which can be seen by the same sign in the percent difference between the two methods in Tables 2 and 3. DFT and DFT+ U predict relatively comparable interlayer relaxation, which is consistent with previous investigations regarding Fe_2O_3 .⁵³

3.3. Stable Surfaces. The stability of the surfaces investigated is dictated by the surrounding environmental conditions. In this work, the environmental parameters considered are oxygen partial pressure and temperature, which are measured by the oxygen chemical potential. A comparison of the calculated geometric structure with experimentally determined values would confirm the validity of this theoretical work; however, since to our knowledge no experimental data exist, surface stability is inferred solely from ab initio thermodynamics. Using ab initio thermodynamics, the free energy of each surface was calculated as a function of the oxygen chemical potential, as shown in Figures 4 and 5, where the surface with the lowest free energy is considered to be the most stable. The limits of the chemical potential are shown by the vertical dashed lines, above which the oxygen condenses on the surface and below which the oxide disassociates. The range of the physically realistic oxygen chemical potentials is greater for DFT+ U , -2.26 eV $< \mu_{\text{O}} - \mu_{\text{ref}} < 0$ eV, as compared to DFT, -1.65 eV $< \mu_{\text{O}} - \mu_{\text{ref}} < 0$ eV ($\Delta\mu \approx 0.6$ eV). In the case of α - Fe_2O_3 , DFT+ U has been reported to predict an oxygen chemical potential regime 0.8 eV greater than that which DFT predicts.^{15,54}

As can be seen in Figures 4 and 5, DFT and DFT+ U predict a crossover point at which different surfaces are stable. DFT predicts this crossover point to occur at $\mu_{\text{O}} - \mu_{\text{ref}} = -1.25$ eV, while DFT+ U predicts this crossover to occur at a more oxygen-rich environment where $\mu_{\text{O}} - \mu_{\text{ref}} = -0.65$ eV. Below the crossover point, DFT and DFT+ U predict the Rh–O- c -cut and O–Rh- r -cutA surfaces to be most stable and independent of the oxygen chemical potential. At low oxygen chemical potentials, oxygen deficit environments exist and favor surfaces with metal terminations. Above the crossover point, DFT predicts similar stability between the O-cut and O–O- r -cutA surfaces while DFT+ U predicts slightly greater stability of the O–O- r -cutA surface as compared to the O- c -cut surface. The surface free energy of the O- c -cut and O–O- r -cutA surfaces decreases with increasing oxygen chemical potential. This seems reasonable since oxygen chemical potentials above the crossover point describe increasingly oxygen-rich environments, which favor oxygen-terminated surfaces. At all chemical potentials, c -cut and r -cut surfaces are pre-

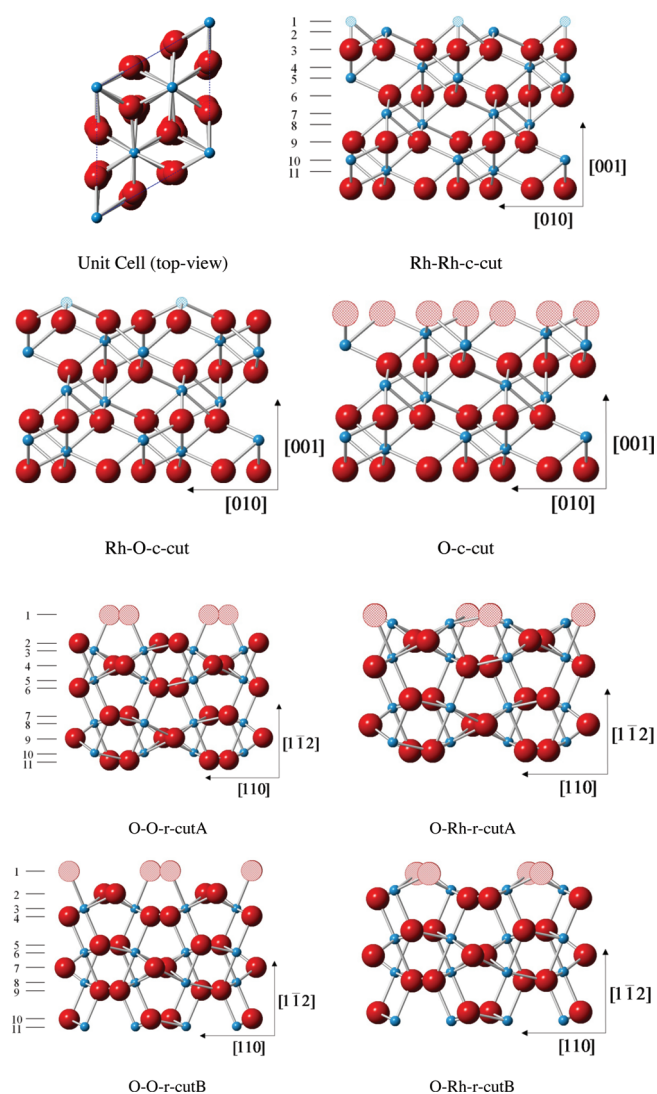


Figure 3. Images of the three c-cut and four r-cut surfaces investigated with each surface termination. Surfaces are referred to by the top two atom layer terminations and by c-cut or r-cut. Rhodium atoms are shown by smaller blue spheres, and oxygen atoms are shown by larger red spheres, while surface atoms are hatched. Layer numbers are references for Tables 2 and 3.

dicted to have similar stability. Therefore, it is possible the chemical nature and structure of a support material may dictate the stability of the c-cut or r-cut surface or that both surfaces may coexist.

The stability of the Rh_2O_3 surfaces is consistent with previous DFT calculations of $\alpha\text{-Fe}_2\text{O}_3$ and $\alpha\text{-Al}_2\text{O}_3$. The c-cut surfaces of $\alpha\text{-Fe}_2\text{O}_3$ were found to have oxygen chemical potential crossover points of $\mu_{\text{O}} - \mu_{\text{ref}} = -0.8 \text{ eV}$ ¹⁶ and -1 eV ,¹⁵ above which the oxygen-terminated surface (analogous to the O-c-cut surface) is the most stable and below which the rhodium-terminated surface (analogous to the Rh-O-c-cut surface) is most stable. This same trend in c-cut surface stability was found in this work, but at a lower crossover oxygen chemical potential, $\mu_{\text{O}} - \mu_{\text{ref}} = -1.25 \text{ eV}$ (Figures 4 and 5). The Gibbs surface free energy is independent of the oxygen chemical potential for the Rh-O-c-cut surface and increases with increasing oxygen chemical potential for the Rh-Rh-c-cut surface (this surface is less thermodynamically favorable over all oxygen chemical potentials), which is the same

behavior for the corresponding c-cut surfaces of $\alpha\text{-Fe}_2\text{O}_3$.^{15,16} DFT+*U* applied to the c-cut surfaces of $\alpha\text{-Fe}_2\text{O}_3$ widened the range of physically realistic oxygen chemical potentials and increased the Gibbs free energy of each surface. For the case of $\alpha\text{-Fe}_2\text{O}_3$, DFT+*U* increased the Gibbs free energy of the oxygen-terminated surfaces more than the Fe-terminated surfaces. This resulted in the Fe-terminated c-cut surface of $\alpha\text{-Fe}_2\text{O}_3$, corresponding to the Rh-O-c-cut surface, being the most thermodynamically stable over nearly the entire range of oxygen chemical potentials.¹⁵ In this work, DFT+*U* predicts a similar trend in the stability of the c-cut surfaces of Rh_2O_3 as compared to c-cut surfaces of $\alpha\text{-Fe}_2\text{O}_3$. DFT+*U* increases the surface free energy of the oxygen-terminated c-cut surface more than the Rh-terminated c-cut surfaces, thus making the Rh-terminated c-cut surface stable over a wider range of oxygen chemical potentials. As a cautionary note, DFT+*U* has been reported to predict with less accuracy, as compared to DFT, the oxygen chemical potential regimes for the stable $\alpha\text{-Fe}_2\text{O}_3$ surface terminations. Although DFT+*U* better predicts bulk properties, DFT may better predict surface stability regimes.⁵⁴

Previous investigations on the clean (nonhydroxylated) r-cut ($1\bar{1}02$) surfaces of $\alpha\text{-Fe}_2\text{O}_3$ and $\alpha\text{-Al}_2\text{O}_3$ show surface stability similar to that of the r-cut surfaces of Rh_2O_3 .^{13,14,18} The r-cut surfaces of $\alpha\text{-Fe}_2\text{O}_3$ exhibit a crossover chemical potential of $\mu_{\text{O}} - \mu_{\text{ref}} = -0.6 \text{ eV}$, below which the corresponding O-Rh-r-cutA surface is more stable and above which the corresponding O-O-r-cutA surface is more stable.¹⁴ This same crossover point occurs at $\mu_{\text{O}} - \mu_{\text{ref}} = -1.1 \text{ eV}$ for Rh_2O_3 (Figure 4). In the case of $\alpha\text{-Al}_2\text{O}_3$, this crossover point is not observed and the corresponding O-Rh-r-cutA surface is the most stable over the entire range of physically realistic oxygen chemical potentials.¹³

The application of the *U* parameter in DFT+*U* slightly changes the predicted stability of the Rh_2O_3 surfaces as can be seen in Figures 4 and 5, namely, by increasing the relative stability of rhodium-terminated surfaces. The addition of the on-site Coulomb term effectively increases the electron-metal cation attractive force, thus reducing the electron interaction with neighboring oxygen atoms. As a result, the weakened metal-oxygen bond favors the stability of metal-terminated surfaces. This effect is seen by the shift to the right of the crossover point in Figure 5.

3.4. Surface Reactivity. In general, the reactivity of a surface can be characterized by the strength of both Lewis and Brønsted acid-base sites, which can be understood, in part, through density of states (DOS) and bond valence analysis. In addition, the work function of a given surface and the charge of the individual atoms on the surface can also be used to determine the trends in the surface reactivity, specifically in regard to the basic sites.

The relative strength of the Lewis acid-base sites is examined using the results of the electronic structure calculations of the various Rh_2O_3 c-cut and r-cut surfaces. The DOS for the Rh-terminated c-cut (Rh-O-c-cut) and O-terminated c-cut surfaces as calculated by DFT are shown in Figure 6a. As can be seen by the figure, both the oxygen-terminated c-cut surface (O-c-cut) and the oxygen-terminated r-cut surface (O-O-r-cutA) have available states at the Fermi energy while Rh-O-c-cut and O-Rh-r-cutA surfaces have available states slightly above the Fermi level. Interestingly, DFT predicts the former c-cut/r-cut surface pair to be similar in stability above the oxygen chemical potential crossover point and the latter c-cut/r-cut surface pair to be similar in stability below the crossover point.

For both the c-cut and r-cut surfaces, there is a clear overlap of Rh d states and O p states at the Fermi level extending into the

Table 2. Surface Relaxation Predictions for the Three c-cut Surfaces Studied^a

layer	Rh–Rh-c-cut				Rh–O-c-cut				O-c-cut			
	Δ		%		Δ		%		Δ		%	
	$U = 0$	$U = 3.5$	$U = 0$	$U = 3.5$	$U = 0$	$U = 3.5$	$U = 0$	$U = 3.5$	$U = 0$	$U = 3.5$	$U = 0$	$U = 3.5$
1–2	0.68	0.56	–50.4	–34.0								
2–3	0.73	0.75	22.5	21.6	0.54	0.57	43.4	40.9				
3–4	1.02	1.02	–7.5	–6.0	1	1.03	–5.8	–7.4	0.77	0.77	18.6	20.0
4–5	0.43	0.4	5.4	5.3	0.27	0.25	39.3	41.4	0.25	0.24	43.7	42.1
5–6	0.99	0.98	–4.3	–1.6	1.08	1.08	–13.9	–12.4	1.2	1.17	–26.7	–22.4
6–7	0.97	0.95	–2.2	1.2	0.94	0.96	1.1	0.3	0.92	0.94	3.2	2.3
7–8	0.44	0.42	3.1	–0.3	0.47	0.43	–4.4	–2.8	0.41	0.4	9.0	4.1
8–9	0.97	0.95	–1.9	1.4	0.93	0.95	1.5	0.6	0.98	0.98	–3.0	–2.1
9–10	0.96	0.95	–1.1	1.3	0.94	0.96	0.7	0.1	0.94	0.96	0.7	0.2
10–11	0.45	0.42	0.7	–0.4	0.46	0.42	–1.3	0.2	0.45	0.42	–0.4	0.3

^a Δ is the absolute vertical distance between layers (\AA), the columns labeled with % give the percent shift in layer position as compared to the corresponding layer position in the bulk oxide, and U is given in electronvolts. Results for DFT and DFT+ U are shown.

Table 3. Surface Relaxation Predictions for the Four r-cut Surfaces Studied^a

layer	O–Rh-r-cutA				O–O-r-cutA				O–O-r-cutB				O–O-r-cutB			
	Δ		%		Δ		%		Δ		%		Δ		%	
	$U = 0$	$U = 3.5$	$U = 0$	$U = 3.5$	$U = 0$	$U = 3.5$	$U = 0$	$U = 3.5$	$U = 0$	$U = 3.5$	$U = 0$	$U = 3.5$	$U = 0$	$U = 3.5$	$U = 0$	$U = 3.5$
1–2					1.27	1.32	16.5	12.4					1.16	1.16	23.6	23.5
2–3	0.37	0.36	2.1	8.1	0.19	0.24	51.1	39.2	0.63	0.62	16.9	17.2	0.56	0.56	–46.4	–42.1
3–4	0.68	0.66	9.2	11.2	0.77	0.83	–2.4	–11.4	0.49	0.48	–28.9	–23.6	0.44	0.43	–14.3	–10.9
4–5	0.77	0.74	–2.1	0.2	0.68	0.73	9.7	1.9	1.44	1.42	5.2	6.3	1.49	1.48	2.0	1.9
5–6	0.41	0.4	–8.6	–2.0	0.4	0.43	–5.8	–10.8	0.37	0.36	2.9	6.9	0.35	0.35	8.1	10.8
6–7	1.49	1.44	1.6	4.6	1.33	1.45	12.7	4.3	0.8	0.79	–6.7	–6.4	0.78	0.78	–4.1	–5.1
7–8	0.37	0.36	2.1	8.0	0.35	0.39	7.0	0.9	0.75	0.74	–0.2	0.1	0.77	0.76	–1.7	–2.7
8–9	0.75	0.72	0.5	2.7	0.68	0.74	9.4	0.1	0.4	0.39	–4.7	–0.4	0.4	0.39	–4.0	–0.9
9–10	0.75	0.72	0.4	2.6	0.68	0.74	10.3	0.8	1.51	1.49	0.6	1.7	1.51	1.5	0.8	0.7
10–11	0.39	0.37	–1.3	4.8	0.36	0.39	6.8	1.2	0.4	0.39	–3.8	0.6	0.39	0.39	–2.5	0.6

^a Δ is the absolute vertical distance between layers (\AA), the columns labeled with % give the percent shift in layer position as compared to the corresponding layer position in the bulk oxide, and U is given in electronvolts. Results for DFT and DFT+ U are shown.

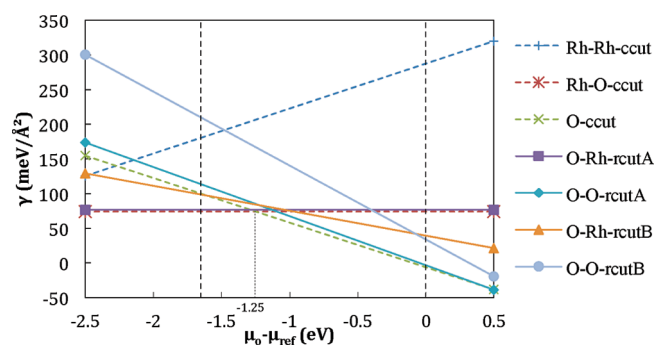


Figure 4. Free energies of the seven surfaces studied for $U = 0$ eV. A crossover point occurs at $\mu_o - \mu_{ref} = -1.25$ eV.

band gap by approximately 0.5 eV. These states represent electron-acceptor sites that result in an increased Lewis acidity for the oxygen-terminated surfaces. The Bader charge is also calculated for

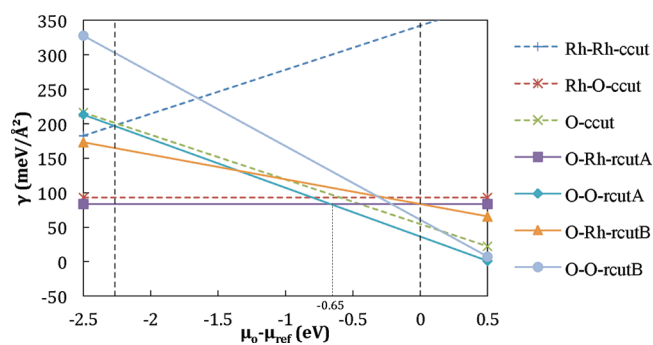


Figure 5. Surface free energies of the seven surfaces studied for $U = 3.5$ eV. A crossover point occurs at $\mu_o - \mu_{ref} = -0.65$ eV.

the surface Rh and O atoms and is shown in Table 4. Within the approach proposed by Bader, the continuous electron density is partitioned into regions bound by the minima of the charge density

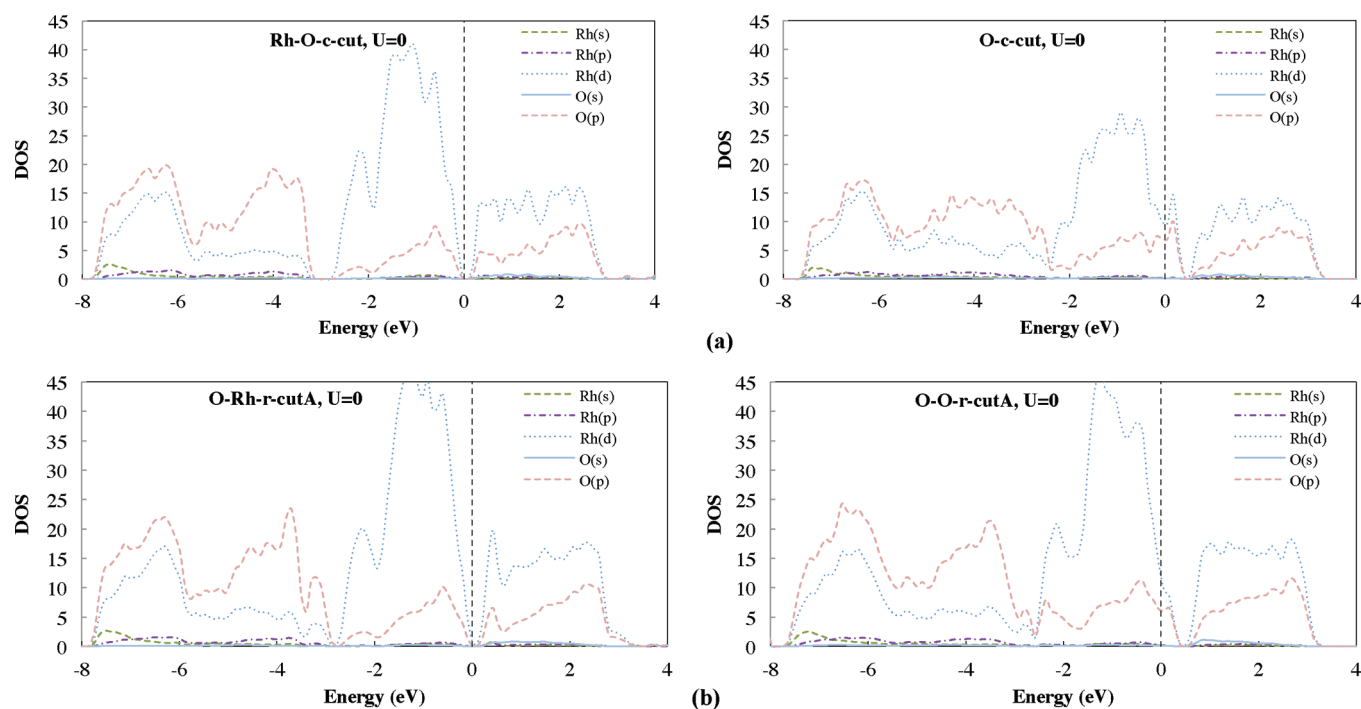


Figure 6. Density of states vs energy plots for the four most stable surfaces with DFT. c-cut surfaces are shown in (a), while r-cut surfaces are shown in (b).

Table 4. Work Function, Bader Charges, and Bond Valence of Rhodium and Oxygen Atoms for the Four Most Thermodynamically Stable Surfaces^a

	Rh–O–c-cut		O–c-cut		O–Rh–r-cutA		O–O–r-cutA	
	DFT	DFT+U	DFT	DFT+U	DFT	DFT+U	DFT	DFT+U
ϕ work function (eV)	4.91	4.85	7.11	6.44	5.07	5.06	7.38	6.84
QB (e), Rh _{top}	1.16	1.25	1.72	1.72	1.31	1.39	1.47	1.50
QB (e), O _{top}	−0.91	−0.97	−0.70	−0.69	−0.98	−1.02	−0.34	−0.29
Δ BV (vu), Rh _{top}	2.178	2.207			2.606	2.625	2.945	2.995
Δ BV (vu), Rh _{second layer}	3.244	3.224	3.587	3.689	3.041	3.035	3.112	3.137
Δ BV (vu), Rh _{third layer}	3.042	3.031	3.454	3.498	3.046	3.013	3.092	3.064
Δ BV (vu), Rh _{fourth layer}	3.022	3	3.198	3.124				
Δ BV (vu), O _{top}	1.858	1.829	1.565	1.566			0.587	0.533
Δ BV (vu), O _{second layer}	1.942	1.96	1.858	1.871	1.686	1.651	1.802	1.779
Δ BV (vu), O _{third layer}	2.015	2.015	2	1.999	1.958	1.957	1.872	1.908

^a Each pair of columns compares DFT with DFT+U predictions.

and then assigned to the individual atoms. A comparison of the Bader charges for the four most thermodynamically stable surfaces shows that the O–c-cut and the O–O–r-cut surfaces have surface Rh atoms with the lowest electron population and respective charges of +1.72e and +1.47e, thus supporting the Rh affinity for electrons. It is interesting to note that the surface oxygen atoms on these two surfaces also have the smallest gain in electron population, and given the available oxygen sites in the gap, these surface oxygen atoms might also act as weak Lewis acid sites. At oxygen chemical potentials above the crossover points, shown in Figures 4 and 5, the O–c-cut and O–O–r-cutA surfaces are close in stability for DFT, with the O–O–r-cutA surface the most stable for the DFT+U case. Both of these surfaces exhibit high Lewis acid reactivity and could explain the high catalytic reactivity in low-temperature N₂O dissociation observed experimentally.^{1–3} Since

oxygen is the basic atom in the nitrous oxide molecule, it is possible that it is the oxygen atom that interacts with the acid sites of the O–c-cut and O–O–r-cutA surfaces.

The results of the DFT+U calculations predict the same trend in reactivity related to the oxygen-terminated surfaces, with the O–c-cut and O–O–r-cutA surfaces possessing the greatest Lewis acid sites corresponding to the surface Rh atoms. However, a comparison of the DOS for DFT+U with that for DFT suggests the relative strength of Lewis acidity is decreased. From Figure 7b, the top of the valence band of the Rh–O–c-cut and O–Rh–r-cutA surfaces is shifted approximately 0.4 eV below the Fermi level for DFT+U compared to DFT. This result is consistent in that the role of the DFT+U correction is to include an extra repulsion term that decreases the affinity for the electrons. Interestingly, this effect is less subtle for the O–c-cut and O–O–r-cutA surfaces.

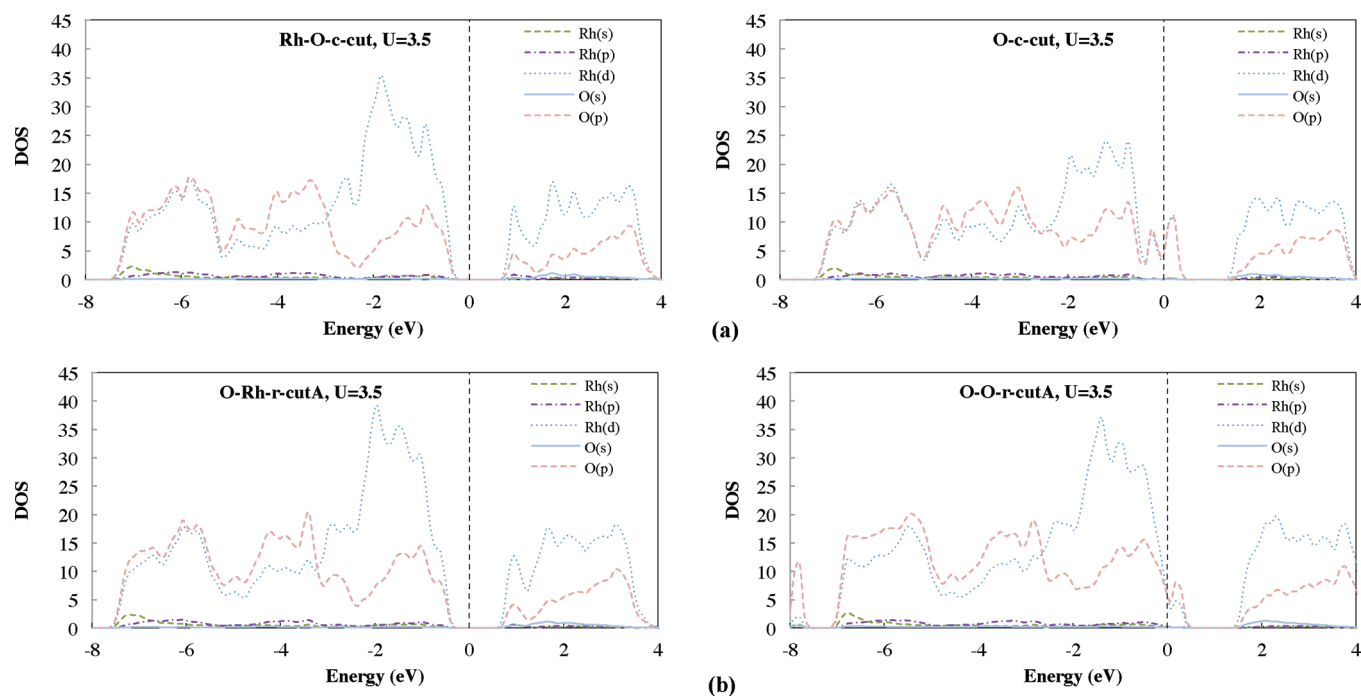


Figure 7. Density of states vs energy plots for the four most stable surfaces with DFT+*U*. c-cut surfaces are shown in (a), while r-cut surfaces are shown in (b).

Although the Lewis acid strength of the surface can be inferred by the location of the empty electronic states of the metal cations, the highest occupied orbitals of the surface oxygen atoms are typically correlated with the Lewis basicity of the surface. Unfortunately, these filled states are less localized, and it is harder to determine the relative strength of the basic sites using only the DOS information. Instead, a better measure of Lewis basicity is to compare the work functions of the various surfaces where surfaces with stronger Lewis base sites will have lower work functions. Here the work function is defined as the difference between the Fermi energy and the energy in the vacuum region of the computational domain, which is a reasonable estimate of the minimum energy necessary to remove an electron from the oxide surface. A lower work function suggests greater ease for a surface to donate electrons and therefore higher reactivity in terms of basicity. For both the c-cut and r-cut surfaces, DFT predicts the Rh-terminated surfaces to have a smaller work function by approximately 2.2 and 2.31 eV than the O-terminated surfaces. This indicates that the Rh-terminated surfaces will have a stronger Lewis basicity. The electronic charge of the surface oxygen atoms on these Rh-terminated surfaces is also the highest compared to the other surfaces. DFT+*U* results in a slightly lower work function as compared to DFT, suggesting stronger Lewis base sites on the surface. As compared to DFT, DFT+*U* predicts similar trends in surface reactivity; however, surface reactivity is predicted to be either similar or slightly greater.

In this initial study, the surfaces were assumed to be dehydrated and the effect of water and/or water vapor in the surrounding environment was not taken into account; therefore, it is not possible to quantify the Brønsted acidity of the surface. However, the bond valence results of this work and previous results of Fe₂O₃ can give insight into how Rh₂O₃ surfaces might react with available protons. Bond valence results for the first several layers of the two most energetically stable c-cut and two most energetically stable r-cut surfaces are shown in Table 4. The surface

oxygen atoms are undercoordinated in both the oxygen-terminated c-cut surface (O-c-cut) and the oxygen-terminated r-cut surface (O–O-r-cutA). These undercoordinated atoms, with a bond valence of approximately 1.57 vu, are relatively unstable and will represent a strong Brønsted base site which can bond with a proton. Future work will focus on investigating the effects of hydroxylation on the surface oxygen atoms. The second layer of the O–Rh-r-cutA surface is also slightly undercoordinated at approximately 1.69 vu for DFT and 1.65 vu for DFT+*U*. Interestingly, the Rh atoms on the Rh–O-c-cut surface are also highly undercoordinated, which makes this surface unstable.

4. CONCLUSIONS

Ab initio thermodynamics and DOS analysis were used with DFT and the DFT+*U* extension to predict the relative stability and reactivity of seven possible surface terminations of Rh₂O₃. The relative stability of each surface was calculated over a range of physically realistic oxygen chemical potentials. DFT and DFT+*U* predict a crossover point below which DFT+*U* predicts slightly greater stability for the O–Rh-r-cutA surface and above which DFT+*U* predicts slightly greater stability for the O–O-r-cutA surface. DFT predicts similar stability between a c-cut and r-cut surface pair above and below this crossover point. Above the crossover point for DFT, the O-c-cut and O–O-r-cutA surfaces are predicted to be comparable in stability, while below the crossover point, the Rh–O-c-cut and O–Rh-r-cutA surfaces are predicted to be comparable in stability. This suggests that either the structure of the oxide support material may dictate the dominant surface or both a c-cut and an r-cut surface may be present as a mixed oxide structure.

DFT+*U* more accurately predicts the band gap and geometric structure of each surface. The two surfaces that DFT and DFT+*U* predict to be most stable above the crossover point (O-c-cut and O–O-r-cutA) also exhibit the greatest Lewis acid reactivity, which

could explain the high reactivity observed by the low-temperature disassociation reaction of nitrous oxide over Rh_2O_3 . These results show that Rh_2O_3 is a promising candidate for the catalytic dissociation of N_2O and provide a foundation for further research toward the development of a kinetic model for N_2O decomposition. Future work will investigate the effect of hydroxylation on surface oxygen atoms in surface stability and structure.

AUTHOR INFORMATION

Corresponding Author

*E-mail: yaniv@stanford.edu.

ACKNOWLEDGMENT

This work was generously sponsored by the Woods Institute for the Environment at Stanford University and the National Science Foundation's Teragrid computation infrastructure.

REFERENCES

- (1) Yuzaki, K.; Yarimizu, T.; Aoyagi, K.; Ito, S.-ichi; Kunimori, K. *Catal. Today* **1998**, *45*, 129–134.
- (2) Kapteijn, F.; Rodriguezmirasol, J.; Moulijn, J. *Appl. Catal.* **1996**, *9*, 25–64.
- (3) Li, Y.; Armor, J. N. *Appl. Catal. B* **1992**, *1*, L21–L29.
- (4) Imamura, S.; Kitao, T.; Kanai, H.; Shono, S.; Utani, K.; Jinai, H. *React. Kinet. Catal. Lett.* **1997**, *61*, 201–207.
- (5) Haber, J.; Machej, T.; Janas, J.; Nattich, M. *Catal. Today* **2004**, *90*, 15–19.
- (6) Uetsuka, H.; Aoyagi, K.; Tanaka, S.; Yuzaki, K.; Ito, S.; S. *Catal. Lett.* **2000**, *66*, 87–90.
- (7) Centi, G.; Galli, A.; Montanari, B.; Perathoner, S.; Vaccari, A. *Catal. Today* **1997**, *35*, 113–120.
- (8) Gustafson, J.; Mikkelsen, a; Borg, M.; Lundgren, E.; Köhler, L.; Kresse, G.; Schmid, M.; Varga, P.; Yuhara, J.; Torrelles, X.; Quirós, C.; Andersen, J. *Phys. Rev. Lett.* **2004**, *92*, 10–13.
- (9) Gustafson, J.; Resta, a; Mikkelsen, a; Westerström, R.; Andersen, J.; Lundgren, E.; Weissenrieder, J.; Schmid, M.; Varga, P.; Kasper, N.; Torrelles, X.; Ferrer, S.; Mittendorfer, F.; Kresse, G. *Phys. Rev. B* **2006**, *74*, 1–7.
- (10) Gustafson, J.; Westerström, R.; Resta, A.; Mikkelsen, A.; Andersen, J. N.; Balmes, O.; Torrelles, X.; Schmid, M.; Varga, P.; Hammer, B. *Catal. Today* **2009**, *145*, 227–235.
- (11) Zhuo, S.; Sohlberg, K. J. *Solid State Chem.* **2006**, *179*, 2126–2132.
- (12) Wold, A.; Arnott, R. J.; Croft, W. J. *Inorg. Chem.* **1963**, *2*, 972–974.
- (13) Mason, S. E.; Iceman, C. R.; Trainor, T. P.; Chaka, A. M. *Phys. Rev. B* **2010**, *81*, 1–16.
- (14) Lo, C.; Tanwar, K.; Chaka, A.; Trainor, T. *Phys. Rev. B* **2007**, *75*, 1–15.
- (15) Rohrbach, A.; Hafner, J.; Kresse, G. *Phys. Rev. B* **2004**, *70*, 1–17.
- (16) Wang, X. G.; Weiss, W.; Shaikhutdinov, S. K.; Ritter, M.; Peterson, M.; Wagner, F.; Schlögl, R.; Scheffler, M. *Phys. Rev. Lett.* **1998**, *81*, 1038–1041.
- (17) Bergermayer, W.; Schweiger, H.; Wimmer, E. *Phys. Rev. B* **2004**, *69*, 1–12.
- (18) Aboud, S.; Wilcox, J.; Brown, G. *Phys. Rev. B* **2011**, *83*, 1–16.
- (19) Tanwar, K.; Catalano, J.; Petitto, S.; Ghose, S.; Eng, P.; Trainor, T. *Surf. Sci.* **2007**, *601*, L59–L64.
- (20) Rollmann, G.; Rohrbach, a; Entel, P.; Hafner, J. *Phys. Rev. B* **2004**, *69*, 1–12.
- (21) Rollmann, G.; Entel, P.; Rohrbach, A.; Hafner, J. *Phase Transitions* **2005**, *78*, 251–258.
- (22) Uozumi, T.; Okada, K.; Kotani, A. *J. Electron Spectrosc. Relat. Phenom.* **1996**, *78*, 103–106.
- (23) Sandratskii, L. M.; Uhl, M.; Kübler, J. *J. Phys.: Condens. Matter.* **1995**, *8*.
- (24) Wang, L.; Maxisch, T.; Ceder, G. *Phys. Rev. B* **2006**, *73*, 1–6.
- (25) Pacchioni, G. *J. Chem. Phys.* **2008**, 128.
- (26) Perdew, J.; Burke, K.; Ernzerhof, M. *Phys. Rev. Lett.* **1996**, *77*, 3865–3868.
- (27) Becke, A. D. *J. Chem. Phys.* **1993**, *98*, 1372.
- (28) Paier, J.; Marsman, M.; Hummer, K.; Kresse, G.; Gerber, I. C.; Angyan, J. G. *J. Chem. Phys.* **2006**, 124.
- (29) Feng, X. B.; Harrison, N. M. *Phys. Rev. B* **2004**, 69.
- (30) Loschen, C.; Carrasco, J.; Neyman, K. M.; Illas, F. *Phys. Rev. B* **2007**, 75.
- (31) Liu, P.; Kendelewicz, T.; Brown, G. E. *Surf. Sci.* **1998**, *412–413*, 315–332.
- (32) Yamamoto, S.; Kendelewicz, T.; Newberg, J. T.; Ketteler, G.; Starr, D. E.; Mysak, E. R.; Andersson, K. J.; Ogasawara, H.; Bluhm, H.; Salmeron, M.; Brown, G. E.; Nilsson, A. *J. Phys. Chem. C* **2010**, *114*, 2256–2266.
- (33) Brown, G. E., Jr. *Surf. Sci.* **2001**, *294*, 67–69.
- (34) Catalano, J. G.; Zhang, Z.; Park, C.; Fenter, P.; Bedzyk, M. J. *Geochim. Cosmochim. Acta* **2007**, *71*, 1883–1897.
- (35) Trainor, T. P.; Eng, P. J.; Brown, G. E.; Robinson, I. K.; Santis, M. D. *Surf. Sci.* **2002**, *496*, 238–250.
- (36) Anisimov, V. I.; Aryasetiawan, F.; Lichtenstein, A. I. *J. Phys.: Condens. Matter* **1997**, *9*, 767–808.
- (37) Hafner, J. *J. Comput. Chem.* **2008**, 29.
- (38) Reuter, K.; Scheffler, M. *Phys. Rev. B* **2002**, 65.
- (39) Sun, Q.; Reuter, K.; Scheffler, M. *Phys. Rev. B* **2003**, *67*, 1–7.
- (40) Wang, X. G.; Chaka, A.; Scheffler, M. *Phys. Rev. Lett.* **200AD**, *84*, 3650.
- (41) Chase, M. W. *NIST-JANAF Thermochemical Tables*, 4th ed.; American Chemical Society: Washington, DC, 1998.
- (42) Pauling, L. *J. Am. Chem. Soc.* **1931**, *53*, 1367–1400.
- (43) Brown, I. D.; Altermatt, D. *Acta Crystallogr., Sect. B* **1985**, *B41*, 244–247.
- (44) Brown, I. D.; Wu, K. K. *Acta Crystallogr., Sect. B* **1976**, *B32*, 1957–1959.
- (45) Brown, I. D.; Shannon, R. D. *Acta Crystallogr., Sect. A* **1973**, *A29*, 266–282.
- (46) de Jonga, B. H. W. S.; Brown, G. E., Jr. *Geochim. Cosmochim. Acta* **1980**, *44*, 491–511.
- (47) Bickmore, B. R.; Rosso, K. M.; Brown, I. D.; Kerisit, S. J. *Phys. Chem. A* **2009**, *113*, 1847–1857.
- (48) Newnham, R. E.; de Haan, Y. M. *Z. Kristallogr.* **2010**, *117*, 235–237.
- (49) Abe, Y.; Kato, K.; Kawamura, M.; Sasaki, K. *Surf. Sci. Spectra* **2001**, *8*, 117.
- (50) Koffyberg, F. *J. Phys. Chem. Solids* **1992**, *53*, 1285–1288.
- (51) Grillo, M. *Phys. Rev. B* **2004**, *70*, 1–6.
- (52) Hiemstra, T.; Venema, P.; Van Riemsdijk, W. H. J. *Colloid Interface Sci.* **1996**, *184*, 680–692.
- (53) Blake, R. L.; Hessevick, R. E.; Zoltai, T.; Finger, L. W. *Am. Mineral.* **1996**, *51*, 123–129.
- (54) Barbier, A.; Stierle, A.; Kasper, N.; Guittet, M. J.; Jupille, J. *Phys. Rev. B* **2007**, *75*, 3–6.